JGR Solid Earth

RESEARCH ARTICLE
10.1029/2024JB029053

Activation of Dissolution-Precipitation Creep Causes Weakening and Viscous Behavior in Experimentally Deformed Antigorite

C. J. Tulley[1,2], L. ten Thij[3], A. R. Niemeijer[3], M. F. Hamers[3], and Å. Fagereng[1]

[1]School of Earth and Environmental Sciences, Cardiff University, Cardiff, UK, [2]Hardie Pacific, Dunedin, New Zealand, [3]HPT Laboratory, Department of Earth Sciences, Utrecht University, Utrecht, The Netherlands

Key Points:

- At 20°C and 500°C antigorite is strain-hardening, develops cataclastic microstructures and has a frictional coefficient of ~0.5
- Samples of antigorite mixed with quartz are strain-weakening, and the friction coefficient decreases from 0.36 at 200°C to 0.22 at 500°C
- The weakness of quartz-antigorite is associated with activation of dissolution-precipitation creep

Correspondence to:
Å. Fagereng,
FagerengA@cardiff.ac.uk

Citation:
Tulley, C. J., ten Thij, L., Niemeijer, A. R., Hamers, M. F., & Fagereng, Å. (2024). Activation of dissolution-precipitation creep causes weakening and viscous behavior in experimentally deformed antigorite. *Journal of Geophysical Research: Solid Earth*, *129*, e2024JB029053. https://doi.org/10.1029/2024JB029053

Received 5 MAR 2024
Accepted 7 AUG 2024

Author Contributions:
Conceptualization: A. R. Niemeijer, Å. Fagereng
Data curation: A. R. Niemeijer
Formal analysis: C. J. Tulley, L. ten Thij, A. R. Niemeijer, Å. Fagereng
Funding acquisition: Å. Fagereng
Investigation: L. ten Thij, A. R. Niemeijer, M. F. Hamers
Methodology: A. R. Niemeijer, M. F. Hamers
Project administration: A. R. Niemeijer, Å. Fagereng
Resources: A. R. Niemeijer
Supervision: A. R. Niemeijer, Å. Fagereng
Visualization: C. J. Tulley, A. R. Niemeijer, Å. Fagereng
Writing – original draft: C. J. Tulley, L. ten Thij, Å. Fagereng
Writing – review & editing: A. R. Niemeijer, M. F. Hamers

Abstract Antigorite occurs at seismogenic depth along plate boundary shear zones, particularly in subduction and oceanic transform settings, and has been suggested to control a low-strength bulk rheology. To constrain dominant deformation mechanisms, we perform hydrothermal ring-shear experiments on antigorite and antigorite-quartz mixtures at temperatures between 20 and 500°C at 150 MPa effective normal stress. Pure antigorite is strain hardening, with frictional coefficient (μ) > 0.5, and developed cataclastic microstructures. In contrast, antigorite-quartz mixtures (10% quartz) are strain weakening with μ decreasing with temperature from 0.36 at 200°C to 0.22 at 500°C. Antigorite-quartz mixtures developed foliation similar to natural serpentinite shear zones. Although antigorite-quartz reactions may form mechanically weak talc, we only find small, localized amounts of talc in our deformed samples, and room temperature friction is higher than expected for talc. Instead, we propose that the observed weakening at temperatures ≥200°C primarily results from silica dissolution leading to a lowered pore-fluid pH that increases antigorite solubility and dissolution rate and thus the rate of dissolution-precipitation creep. We suggest that under our experimental conditions, efficient dissolution-precipitation creep coupled to grain boundary sliding results in a mechanically weak frictional-viscous rheology. Antigorite with this rheology is much weaker than antigorite deforming frictionally, and strength is sensitive to effective normal stress and strain rate. The activation of dissolution-precipitation in antigorite may allow steady or transient creep at low driving stress where antigorite solubility and dissolution rate are high relative to strain rate, for example, in faults juxtaposing serpentinite with quartz-bearing rocks.

Plain Language Summary Some major, plate-boundary fault zones are very weak, and in some places this is thought to be because they contain the mineral serpentine. Antigorite is a common form of serpentine at depth, but in many rock deformation experiments, antigorite is found to be relatively strong. In natural fault zones, however, antigorite can be highly deformed at seemingly low stress. The motivation for this study was to explore whether antigorite can be weak also in the laboratory. Because laboratory experiments occur relatively fast, the mechanism of deformation may be different from in nature. To address this, we mixed antigorite with quartz, which changes the pH and promotes dissolution of antigorite. We found that when deforming antigorite mixed with quartz, the experimental fault was very weak, because the dissolution of antigorite removed sticking points - a process that is also documented in natural faults. The experiments also produced minor talc, from the reaction of antigorite with quartz, but too little to affect strength. We suggest that it is the activation of dissolution and precipitation of antigorite which allows deformation of major serpentine-bearing faults at low stress at temperatures of several hundred degrees Celsius.

1. Introduction

The high-temperature serpentine polymorph, antigorite, has been inferred to contribute substantially to the weakness of subduction interfaces, and may determine fault slip style where present (Peacock & Hyndman, 1999; Wada & Wang, 2009; Wang et al., 2020). Contrary to this view, the strength of antigorite is typically quite high in deformation experiments (e.g., Hirauchi et al., 2020; Shao et al., 2021), particularly relative to other serpentine varieties (e.g., Moore & Lockner, 2013; Reinen et al., 1994; Takahashi et al., 2011; Tesei et al., 2018). To explain this discrepancy, it is commonly inferred that weak antigorite-dominated serpentinite faults will slip predominantly through steady or transient viscous creep, accommodated at the microscale by dislocation creep (e.g., Goswami & Barbot, 2018; Hilairet et al., 2007; Hirauchi et al., 2021). However, some field observations (Tulley et al., 2022; Wassmann et al., 2011) and laboratory results (Chernak & Hirth, 2010; Hansen et al., 2020) suggest

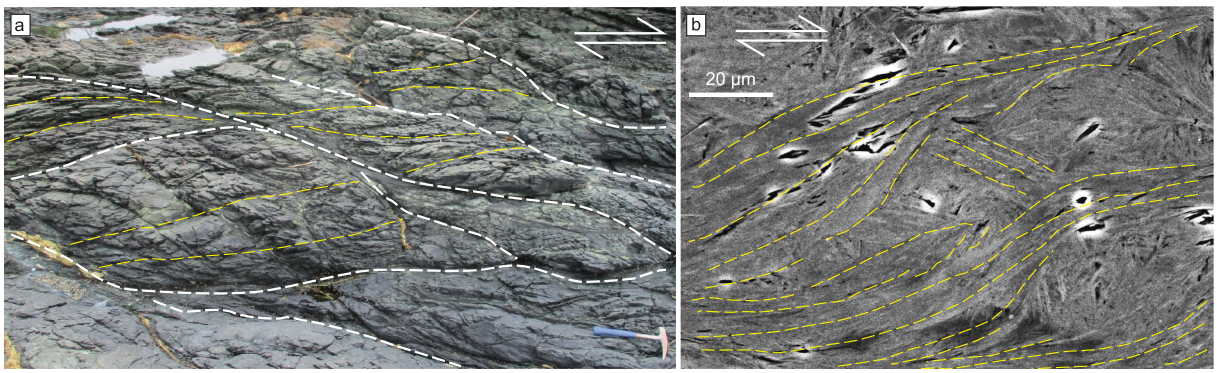

Figure 1. Structures observed in naturally deformed antigorite in the Nishisonogi metamorphic rocks described in detail by Tulley et al. (2022). At the mesoscale (a: field photograph), foliations define an S-C′ structure, where S foliations (yellow lines) merge into C′ shear surfaces (white lines). At the microscale (b: backscattered electron image), foliations (dashed yellow lines) are defined by aligned antigorite long axes, and separate relatively competent clasts of interlocking antigorite crystals.

that dislocation creep in antigorite may accommodate only minor strains at tectonic strain rates. Therefore we aim to test whether antigorite can deform by steady creep, at low stress, in a laboratory environment, and what mineral-scale mechanism(s) accommodate a large strain.

Structural observations from subduction-related exhumed shear zones have provided opportunities to constrain deformation mechanisms at natural strain rates (Figure 1). Well-developed foliations and folds (Tarling et al., 2019; Tulley et al., 2022) suggest that antigorite behaves viscously at greenschist and amphibolite facies conditions. Observations of crystal distortions suggest the operation of dislocation-related deformation mechanisms (Padrón-Navarta et al., 2012; Tulley et al., 2022), and microstructures indicating local dissolution and precipitation suggest that antigorite deformation also occurs by dissolution-precipitation creep (Liu et al., 2020; Tulley et al., 2022; Wassmann et al., 2011). Microstructures characteristic of a particular deformation mechanism do not necessarily constrain which mechanism controls strength, since several mechanisms may operate simultaneously (e.g., Bos & Spiers, 2002; Warren & Hirth, 2006). However, antigorite microstructures from the Nishisonogi metamorphic rocks (Figure 1), which are inferred to have deformed along a subduction plate boundary at ∼500°C, are consistent with viscous deformation dominated by dissolution-precipitation creep, with only very minor strains accommodated by dislocation creep (Tulley et al., 2022). A similar conclusion was drawn from serpentinites deformed at subduction-related, high pressure (2 ± 0.5 GPa) - low temperature (550 ± 50°C) conditions in the Zermatt-Saas zone of the Western European Alps (Wassmann et al., 2011).

Laboratory experiments, conducted at a few GPa confining pressure and temperatures 300–600°C, allow direct measurements of antigorite rheology. However, with the exception of experiments by Burdette and Hirth (2022) who achieved strain rates as low as 10^{-9} s^{-1}, these experiments are performed at strain rates $\sim10^{-5}$ s^{-1}, many orders of magnitude greater than inferred for natural shear zones (commonly $\leq10^{-12}$ s^{-1}; Fagereng & Biggs, 2019). If data from antigorite deformation experiments are fitted to a power-law, stress exponents are generally >10 (Burdette & Hirth, 2022; Proctor & Hirth, 2016; Shao et al., 2021), consistent with dislocation glide or semi-brittle behavior (Burdette & Hirth, 2022; Chernak & Hirth, 2010).

Friction coefficients obtained during laboratory deformation at lower confining pressures (typically around 0.1 GPa) are commonly in the range 0.5–0.85 (Moore & Lockner, 2013; Reinen et al., 1994; Takahashi et al., 2011), which is similar to most crustal rocks ($0.6 < \mu < 0.85$; Byerlee, 1978). In contrast with natural antigorite shear zones that are m–km wide and typically dominated by distributed, viscous deformation (Tarling et al., 2019; Tulley et al., 2022; Wassmann et al., 2011), laboratory shear zones are narrow within the deformed sample with cataclastic microstructures developed (Chernak & Hirth, 2010; French et al., 2019; Moore & Lockner, 2013; Proctor & Hirth, 2016). The low dehydration temperature of antigorite (∼500–700°C; Ulmer & Trommsdorff, 1995) restricts the ability to trade off temperature for strain rate. As a result, at typical laboratory strain rates, the driving stress required for temperature-sensitive viscous creep may be close to or greater than frictional strength. This might explain why frictional behavior is commonly observed in experiments, while naturally developed microstructures typically suggest a viscous mechanism.

In contrast to previous laboratory studies on antigorite, Moore and Lockner (2013) show that the strength of antigorite sheared against quartz-rich rocks is highly temperature-sensitive. The temperature sensitivity in these experiments is attributed to chemical reactions that enhance the rates of solution-transfer processes. Reaction between serpentine and quartz, itself a solution-transfer process, leads to the formation of mechanically weak talc (Koons, 1981; Mori et al., 2007), and talc has therefore been interpreted to control the rheology of quartz-serpentine mixtures (Hirauchi et al., 2013), particularly in the longer term (Moore & Lockner, 2013). Following Moore and Lockner (2013), we conduct experiments by adding ≤10% quartz to the antigorite samples to investigate the mechanism responsible for temperature-dependent weakening of antigorite-quartz mixtures, specifically whether the enhanced dissolution-precipitation kinetics may allow for dissolution-precipitation creep to operate at laboratory strain rates. Our results extend those of Moore and Lockner (2013) to higher temperatures and strains, and based on our laboratory experiments we speculate on the potential role of dissolution-precipitation creep in natural serpentinite shear zones.

2. Methods

2.1. Starting Material

The antigorite used in the experiments has a greenish color, contains minor magnetite and shows an intense foliation. The composition of the antigorite was measured by energy-dispersive spectroscopy (EDS, see Section 2.3 for details) on 44 antigorite grains. The antigorite has (by weight): 43.1% SiO_2, 37.2% MgO, 4.3% FeO, 1.5% Al_2O_3, and 12.8% H_2O, with standard deviations less than 1%. Powdered quartz with a grain size <15 μm was sourced from the US Silica Company (product name: min-u-sil 15). The antigorite was reduced to grain size fractions 45–106 μm and 25–45 μm by crushing using a mortar and pestle, followed by sieving.

2.2. Experimental Procedure

The experiments were performed in a hydrothermal rotary shear apparatus in the HPT Laboratory, Utrecht University, as described in detail by Niemeijer et al. (2008). Each experiment used ∼0.5 g of powdered material, corresponding to an initial sample thickness of ∼1 mm. With the sample in place between the pistons, the piston assembly is lowered into a pressure vessel filled with distilled H_2O, which serves as the pore fluid. The pressure vessel is placed in an Instron loading frame and then engaged with the rotary forcing assembly. The sample is then heated and pressurized to the experimental conditions, before normal stress is applied. A pressure-compensation system allows the applied normal force to be transferred completely to the sample, minus a small amount of force supported by the internal piston seals. Once at the desired temperature, pressure and normal stress, the sample was left for ∼1 hr to allow for compaction and equilibration of pressure and temperature, before initiating shearing. During the experiments, samples are sheared to a total shear displacement x_{tot} at a range of velocities (see Table 1) to test both steady-state and velocity-dependent friction. Shear stress is measured with a resolution of 0.004 MPa, and normal stress is held constant to within 0.05 MPa. Fluid pressure is measured with a resolution of 0.005 MPa. Shear displacement is measured using a potentiometer with a resolution of $3 * 10^{-5}$ mm. The temperature of the sample is recorded by a thermocouple in contact with the piston assembly close to the sample layer, which is accurate to within 1°C.

Each experiment consisted of a "run-in" phase where the sample was sheared at 1 μm/s for 1 mm, after which the velocity was reduced to 0.01 μm/s for at least 1 mm of displacement or longer if friction was not steady (see Table 1). We take the friction coefficient at the end of the 0.01 μm/s phase as the sample friction coefficient. After shearing at 0.01 μm/s, velocity-step tests were conducted (Table 1). At the end of each experiment, shear stress was removed, followed by cooling to room temperature and removal of fluid pressure and normal stress within ∼30 min. The pistons were then separated, and fragments of the ring-shaped sample were retrieved and set in epoxy.

Three types of experiments are reported (Table 1). (a) Experiments deforming both antigorite-only and antigorite-quartz mixtures with 10% quartz, with an initial antigorite grain size of 45–106 μm, at temperatures between 20 and 500°C; (b) experiments deforming antigorite-quartz mixtures with 5% and 10% quartz, initially at 500°C then at 20°C, using initial antigorite grain sizes 45–106 and 25–45 μm; and (c) a single experiment (u1185) deforming antigorite +10% quartz at 500°C with varied normal stress. Experiment set (a) is designed to investigate the sensitivity of strength to temperature and the presence of quartz, and each experiment was conducted at a constant temperature. Experiment set (b) is designed to investigate the sensitivity to antigorite grain size, and by reducing temperatures to room temperature during the experiment, test whether processes occurring at 500°C (such as talc

Table 1
Details of the Experiments

Exp. ID	wt% quartz	*d* antigorite (μm)	*T* (°C)	*v* (μm/s)	*μ* (x in mm)	x_{tot} (mm)
u860	10	45–106	400	1-0.01-0.03-0.01	0.27 (3.0)	4.7
u863	10	45–106	300	1-0.01-0.03	0.32 (5.5)	6.5
u864	10	45–106	200	1-0.01-0.03-0.01	0.36 (7.1)	9.0
u865	10	45–106	500	1-0.01-0.03	0.22 (3.2)	4.9
u866	10	45–106	20	1-0.01-0.03-0.1-0.3-1	0.47 (4.5)	9.8
u867	0	45–106	300	1-0.01-0.03	0.51 (3.5)[a]	5.2
u870	5	25–45	500 | 20	1-0.01-0.03-0.01-0.03-1	0.22 (2.9)	7.9
u885	5	45–106	500 | 20	1-0.01-0.03-0.01	0.33 (4.4)	5.3
u888	10	45–106	500 | 20	1–0.01	0.24 (2.5)	3.4
u894	0	45–106	500	1-0.01-0.03	0.63 (2.9)[b]	4.4
u899	10	25–45	500 | 20	1–0.01	0.22 (3.8)	5.5
u1185	10	45–106	500	1–0.01	0.18 (2.7)	3.5

Note. d = grain size, T = temperature, v = imposed slip velocity, μ = steady state friction, x is the displacement at which μ was measured, and x_{tot} is the total displacement in the experiment. [a]Friction did not reach steady state. [b]Value at peak of stick-slip.

formation) had a substantial influence on the deformed sample's strength at room temperature. Experiment sets (a) and (b) were performed at constant effective normal stress of 150 MPa. To test for normal stress dependence, during experiment u1185 normal stress was stepped incrementally from 50 to 200 MPa and friction allowed to recover after each step.

2.3. Sample Analyses

Images of microstructures in deformed sample fragments were taken from standard 30 μm thin sections cut parallel to the shearing direction and perpendicular to the shearing plane. Back-scattered electron images and EDS maps were collected using a Zeiss EVO 15 scanning electron microscope (SEM) and a ThermoFisher Talos F200X scanning transmission electron microscope (STEM), used in STEM mode, in the Electron Microscopy Centre at Utrecht University. For SEM analysis, a several nm thick layer of carbon was applied to the surface to prevent charging. For STEM, a focused ion beam cut was made from one of the normal thin sections. For Fourier transform infrared (FTIR) spectroscopy, a small amount (~0.003 g) of sample fragments and a reference talc sample were gently disaggregated using a pestle and mortar, mixed with 0.5 g of KBr powder and pressed into a disc at a pressure of 400 bar. This disc was analyzed in a Jasco FT/IR-470 Plus spectroscope with a spectral resolution of 4 cm^{-1} (wavenumber) and in IR transmission mode.

3. Results

3.1. Mechanical Data

We first present frictional behavior at constant temperatures from room temperature through to 500°C (Figure 2a). At room temperature, antigorite with 10% quartz is slightly strain-weakening after reaching a peak friction of $\mu \sim 0.5$ at ~1.5 mm displacement. After 4 mm displacement, the friction is roughly steady, at $\mu = 0.47$. In antigorite-only experiments at 300 and 500°C gradual strain-hardening occurs after ~1 mm displacement. These experiments at 300 and 500°C reach frictions of $\mu = 0.51$ at ~3.5 mm displacement and $\mu = 0.63$ at ~2.9 mm displacement, respectively, both of which exceed those measured for antigorite with 10% quartz at room temperature. The antigorite-only experiment at 500°C shows intense fluctuations in friction coefficient after ~1 mm displacement, reflecting stick-slip behavior (Figure 2a).

In contrast to the antigorite-only experiments, antigorite-quartz mixtures are strain-weakening after reaching a peak strength of $\mu \sim 0.5$, and the rate of strain-weakening is greater at higher temperatures. The antigorite-quartz mixtures are consistently weaker at temperatures ≥200°C than at room temperature. The approximately steady-

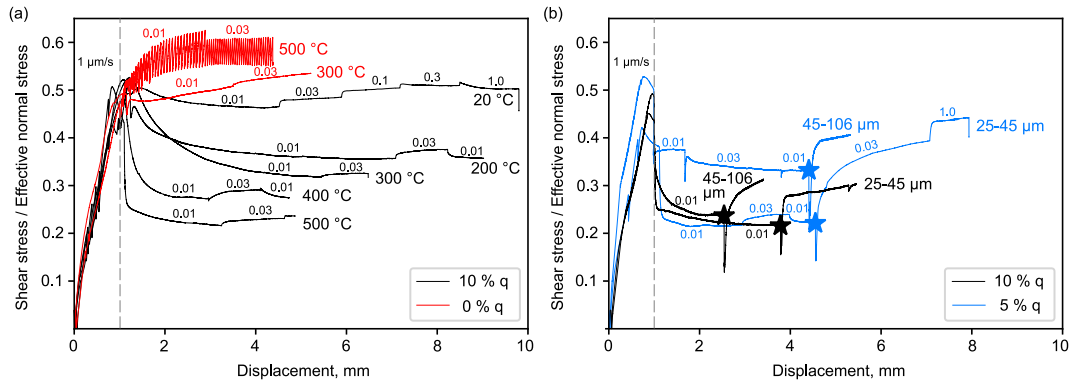

Figure 2. Friction versus displacement for antigorite and antigorite-quartz experiments. Some minor stick-slips may be seen in the loading phase to peak stress. (a) Shows constant-temperature experiments, while (b) shows experiments where temperature was initially 500°C but lowered to room temperature at the displacements indicated by stars. Small numbers along the curves indicate slip velocity in μm/s, after the initial slip at 1 μm/s for 1 mm indicated by the vertical dashed gray line. Labels at the right-hand end of curves in panel (a) are the constant temperature in each experiment, and in panel (b) are antigorite grain size. "q" = quartz content.

state μ at the end of the 0.01 μm/s phase decreases gradually from 0.36 to 0.22 as temperature is increased from 200 to 500°C (Figure 2a). No stick-slip behavior is seen in the antigorite-quartz samples after ∼1 mm displacement.

We also tested four samples at 500°C followed by further shear at room temperature (Figure 2b). Experiment u870, with an initial antigorite grain size 25–45 μm and quartz fraction 5 wt.%, reached a ∼steady-state friction coefficient $\mu = 0.22$ after 2.9 mm displacement at 0.01 μm/s at 500°C. After exceeding 4 mm displacement, lowering temperature to room temperature caused an increase in friction, first at 0.01 μm/s then reaching $\mu \approx 0.38$ at 0.03 μm/s (Figure 2b). Using the change in friction in the velocity step from 0.03 to 1 μm/s ($\Delta\mu = 0.06$), assuming rate-and-state friction holds, we can calculate an $(a - b)$ value of 0.017, which gives $\mu \sim 0.36$ at 0.01 μm/s and room temperature. The same temperature-step routine was applied to experiment u885, which used an initial antigorite grain size 45–106 μm and quartz fraction of 5 wt.%. This experiment reached a ∼steady-state friction coefficient $\mu = 0.33$ at 500°C, after which lowering temperature to room temperature caused a sharp increase in μ to 0.4, followed by gradual strain-hardening (Figure 2b). These results indicate that finer-grained mixtures are weaker at elevated temperature, and remain slightly weaker than the coarser-grained mixtures at room temperature, but independent of initial grain size a strengthening to μ above 0.35 occurs at room temperature. The same pattern of increased strength at room temperature ($\mu > 0.3$) compared to 500°C ($\mu = 0.22$–0.24) is observed for experiments with 10 wt.% quartz, although the grain-size effect is less pronounced and room temperature friction is lower than with 5% quartz (Figure 2b).

In the normal stress stepping experiment, after run-in, the friction coefficient (defined as shear stress/normal stress) drops and then recovers to the steady state value after each up-step in normal stress (Figure 3a). Shear stress increases linearly with increase in normal stress, with an R^2 value of 0.999. Assuming Mohr-Coulomb mechanics, the steady state friction coefficient determined by plotting shear stress against normal stress, at 500°C, is 0.159 ± 0.001 (Figure 3).

3.2. Microstructures and FTIR Spectroscopy

At low magnification in a petrographic microscope, with the sensitive tint plate inserted, a variation in fabric development is clear between experiments at room temperature and 500°C, and between experiments with and without quartz (Figure 4). At room temperature, in a sample with 10% quartz, a subhorizontal fabric developed by a preferred orientation of crystal long axes subparallel to the horizontal shear plane (Figure 4a). There is, however, only a relatively weak consistency in the color of the crystals under the sensitive tint plate. In a sample with 10% quartz deformed at 500°C, an S-C-type fabric developed, with both an inclined antigorite fabric consistent with dextral shear and a subhorizontal fabric (Figures 4b and 4c). The inclined S-fabric is characterized by a consistent color under the tint plate (Figure 4b), which is less developed in the subhorizontal foliation in areas of less developed S-C fabric (Figure 4c). In the sample with only antigorite deformed at 500°C, there is also an inclined fabric, but it

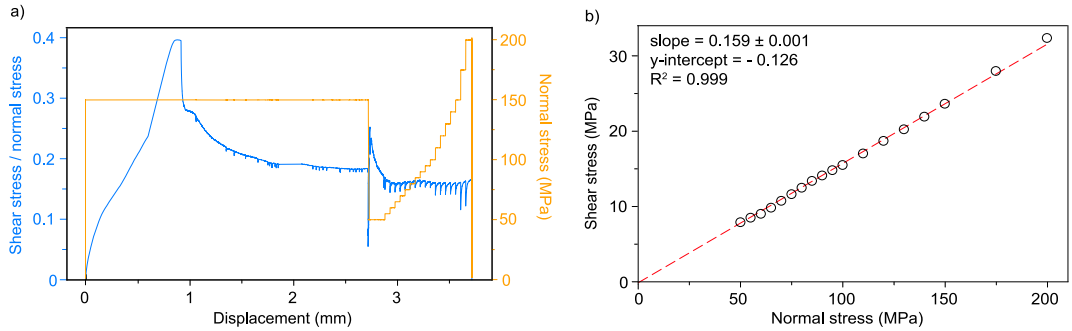

Figure 3. Stress stepping experiment using antigorite with 10% quartz and 45–106 μm grain size, deformed at 500°C. Panel (a) shows the development of shear stress over normal stress with displacement (blue line) compared to the applied normal stress (orange line). In panel (b) we plot shear stress against normal stress and fit a linear relation with slope 0.16.

has a wavy appearance and spans the thickness of the recovered sample (Figure 4d). Dilatant cracks have developed parallel to the foliation. The color under the tint plate is relatively uniform in the fabric-defining grains.

Backscattered electron images of the antigorite-only sample deformed at 500°C show large subrounded to angular clasts, with short axis lengths of several tens of μm, in a matrix of substantially smaller grains that are commonly

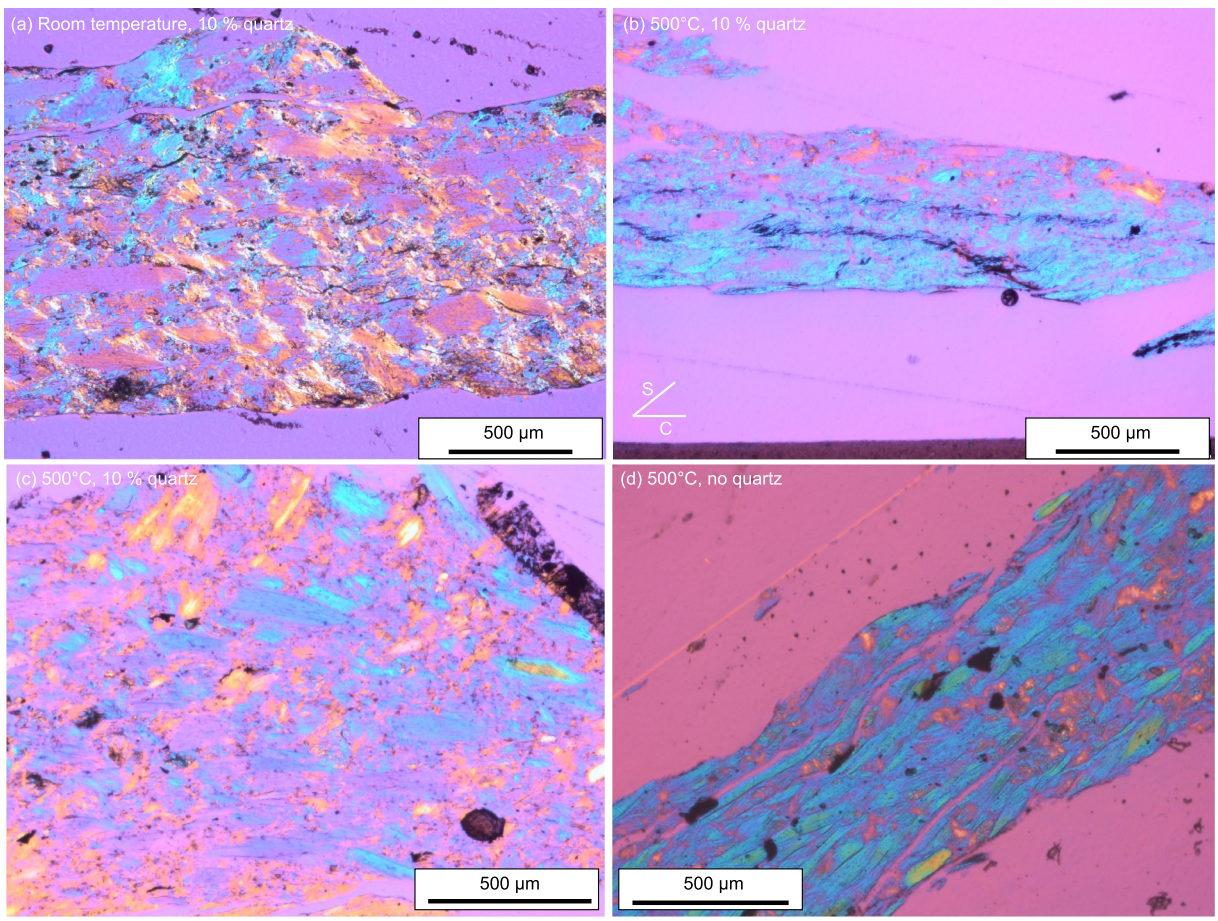

Figure 4. Photomicrographs of deformed samples with the sensitive tint plate inserted. The shear sense is dextral. (a) Sample of antigorite mixed with 10% quartz deformed at room temperature (experiment u866). There is a general trend of long axes aligned parallel to the horizontal shear plane. (b) Sample of antigorite mixed with 10% quartz deformed at 500°C (experiment u865). Here there is also an inclined "S" fabric in a consistent color. (c) Same experiment as (b) but a recovered fragment that preserves a dominant horizontal fabric, parallel to the shear plane, and with several grains oriented in other directions. (d) Sample of antigorite without quartz, deformed at 500°C (experiment u894), where a wavy fabric has developed at a low angle to the shear plane.

<5 μm (Figure 5a). Clast edges are sharp and intragranular fractures are pervasive and especially common parallel to the shear plane. The long axes of the larger clasts generally lie at a low angle to the shear plane, but finer-grained clasts within the matrix form a fabric wrapping around larger clasts (Figure 5a). This foliation is defined by antigorite long axis alignment, and is generally wavy and kinked (Figure 5a). Based on Mg and Si element maps, no compositional variation has developed during the experiment (Figures 5b and 5c).

In contrast, antigorite-quartz experiments, also at 500°C, produced a relatively planar, continuous foliation within some elongate antigorite, separating rounded to subrounded antigorite clasts (Figure 5d). The antigorite clasts are less elongate than in the antigorite-only sample, and the edges are poorly defined, maybe because the sample is relatively cohesive and the fine grained, cataclastic matrix seen in the antigorite-only sample has not developed. The planar to anastomosing foliation around the larger antigorite clasts is defined by a preferred orientation of elongate clasts and the cleavage within them. There is a slight compositional variation, where some (but not all) foliated areas are enriched in silicon and depleted in magnesium, relative to the antigorite clasts (Figures 5e and 5f). Quartz grains are visible within areas separating antigorite clasts, and are rounded to subrounded and typically <10 μm in diameter (vs. a starting grain size of <15 μm).

Deformation of antigorite +10% quartz at room temperature led to microstructures similar to that of antigorite-only at 500°C, dominated by fracture and comminution (Figure 5g). The quartz is visible as lighter grains in the backscatter electron image (Figure 5g) and is angular. This quartz shape differs from that in the antigorite + quartz sample deformed at 500°C, where the quartz is rounded, locally asymmetric, and locally including small pits (Figure 5h).

In experiment set (b), which tested for effects of grain-size, different microstructures developed for initial antigorite grain-sizes of 25–45 μm and 45–106 μm in the samples with 5% quartz (Figure 6). At the finer grain size, an undulating foliation developed by preferred orientation of lenticular antigorite grains, typically with an internal cleavage subparallel to the foliation (Figure 6a). This is similar to scaly foliation commonly seen in fine grained phyllosilicates. There is no clear variation in composition within this sample detectable with either Si or Mg EDS maps (Figures 6b and 6c). In contrast, the coarser-grained sample retains some large antigorite grains that lack internal cleavage visible in the cut sample, and these large grains are surrounded by a matrix of foliated antigorite (Figure 6d). Here, enrichment in Si is detectable in the upper part of the sample, particularly in the stress shadows of large antigorite grains (Figures 6e and 6f). Recall that at 500°C, the finer-grained sample that developed a scaly cleavage was weaker than the coarser-grained sample. Both samples saw a marked increase in strength at room temperature, where the finer grained sample remained slightly weaker than the coarser grained sample (Figure 2b).

Despite the presence of quartz in the starting material, and the expected reaction of serpentine and quartz to form talc and water, quartz is scattered and talc is not apparent in backscattered electron images of the antigorite-quartz sample deformed at 500°C (Figures 5d–5f). In EDS maps obtained in the STEM, the concentration of Si is locally elevated within some areas. Such areas include a relatively weakly foliated area, where the foliation has some kinks and bends and wraps around an antigorite clasts, distinct from very well foliated antigorite (Figures 7a and 7b). Similar texture and Si-enrichment is also seen in fine grained stress shadows adjacent to some antigorite grains (Figures 7c and 7d).

To determine whether talc formed during our experiments at 500°C, we collected FTIR spectra of deformed antigorite, antigorite-quartz mixtures and a talc reference sample. These spectra show distinct peaks near ∼600, ∼1,000, and ∼3,500 cm^{-1} (Figure 8), consistent with previous analyses of antigorite (Balan et al., 2021) and talc (Parry et al., 2007). Spectra from u885 and u865, which contained 5 and 10 wt% quartz, respectively, show subtle peaks at 670 and 3,430 cm^{-1}, that are not present in antigorite spectra (Figure 8). These spectra occur at the same position as peaks in the talc spectrum, suggesting that some talc formed from antigorite-quartz mixtures; however, the peaks are subtle so the amount of talc is relatively small.

4. Discussion

4.1. Dominant Deformation Mechanisms

Samples from antigorite-only experiments at 500°C show a large scale microstructure with wavy, kinked foliation (Figure 4d), at the SEM scale defined by large grains with ragged edges that are intensely fractured and hosted in a matrix of substantially finer grains (Figure 5a). At the SEM scale, microstructures typical of intense fracturing

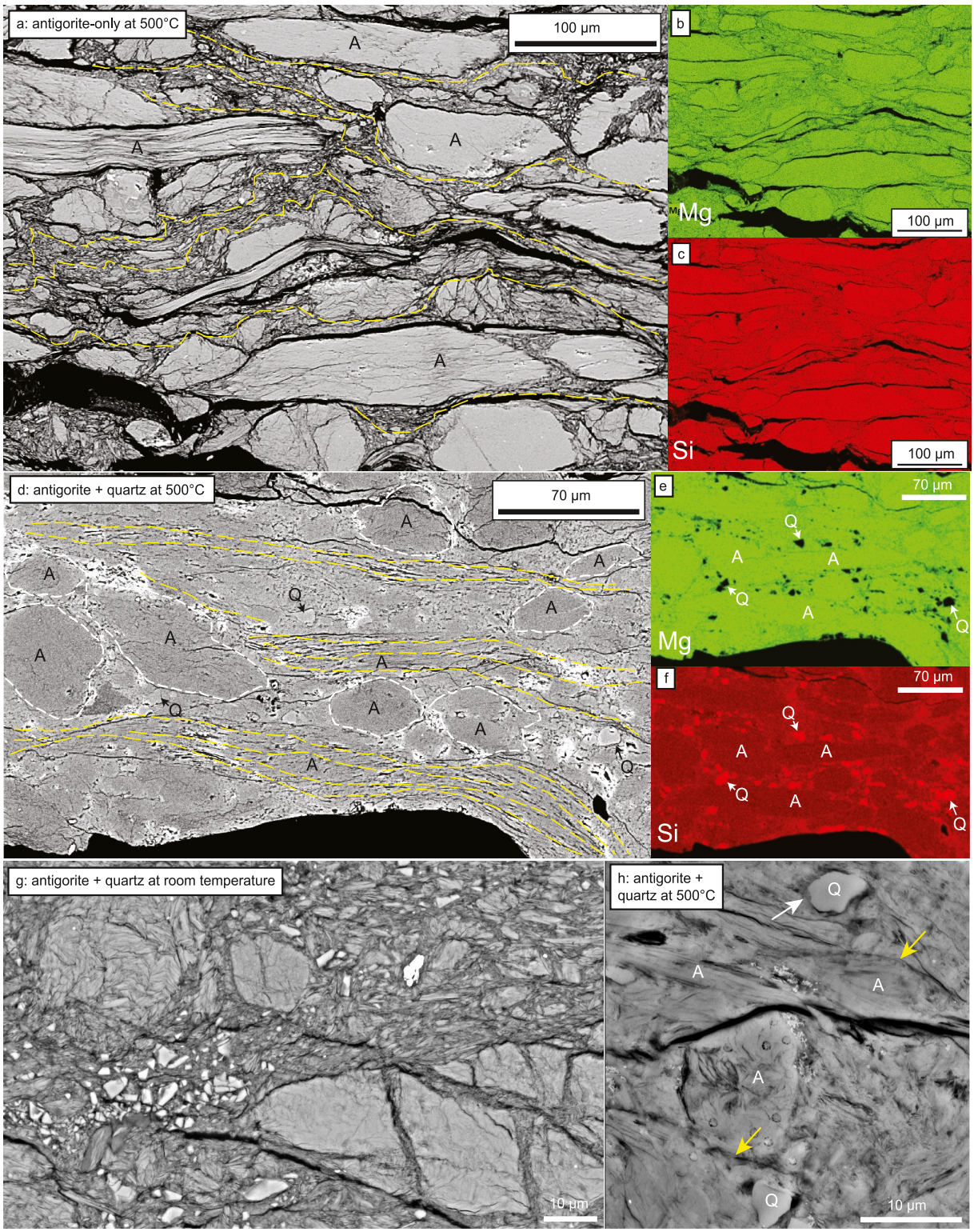
a: antigorite-only at 500°C
100 µm
A
b
Mg
100 µm
c
Si
100 µm
d: antigorite + quartz at 500°C
70 µm
Q
e
70 µm
Mg
f
70 µm
Si
g: antigorite + quartz at room temperature
10 µm
h: antigorite + quartz at 500°C
10 µm

Figure 5.

also developed in antigorite + quartz samples deformed at room temperature (Figure 5g); however, at the larger scale, the foliation developed in these room temperature experiments is more planar, and there is less development of a preferred crystal orientation (Figure 4a). These microstructures are consistent with cataclasis being an important deformation mechanism (e.g., Blenkinsop, 2007, Chapter 2). Similar SEM-scale antigorite microstructures are reported by Chernak and Hirth (2010) and French et al. (2019), who also interpret cataclasis to be an important deformation mechanism. Friction coefficients for antigorite deformed at 500 and 300°C are within the range of previous values obtained at room temperature ($0.5 < \mu < 0.85$; Moore & Lockner, 2013; Reinen et al., 1994; Takahashi et al., 2011; Tesei et al., 2018), consistent with a frictional mechanism in our antigorite-only experiments at elevated temperatures. Stick-slip observed at 500°C implies unstable frictional sliding, as also seen in other experiments (Okazaki & Katayama, 2015; Takahashi et al., 2011) and potentially explained by frictional sliding on shear cracks parallel to the antigorite basal plane (Hansen et al., 2020). The room temperature experiment on antigorite + quartz was slightly weaker ($\mu = 0.47$) than the above-mentioned past room temperature values for antigorite-only.

The antigorite-quartz experiment at 500°C did not show stick-slip after peak stress, but instead displayed time-dependent weakening, and increase in strength at velocity up-steps (Figure 2). This experiment produced an S-C fabric at the thin section scale (Figure 4b), and an SEM-scale microstructure with well-developed, coherent foliation that anastomoses around antigorite clasts (Figure 5d). This microstructure is similar to microstructures observed in natural, greenschist to amphibolite facies shear zones (e.g., Figure 1b), where dissolution-precipitation creep has been demonstrated to be an important deformation mechanism (Tulley et al., 2022; Wassmann et al., 2011). A similar microstructure was seen in the set (b) experiments with variable grain size and 5% quartz, but there is a better developed, connected, scaly foliation developed in the finer-grained sample (Figure 6a) compared to the coarser-grained sample (Figure 6d). If dissolution-precipitation creep is important, this is consistent with lower strength in the finer-grained sample at 500°C as diffusion length scales are short compared to around large grains disrupting the foliation in the coarser grained sample. In the set (b) experiments with 10% quartz, the grain size dependence was less pronounced, and both the coarse- and fine-grained samples had similar strength to the fine-grained sample with 5% quartz. We speculate that this may be because more quartz allowed more efficient dissolution-precipitation creep and foliation development, and therefore weakening of both samples with only minor difference in relative strength.

The strength of antigorite-quartz gouges is inversely proportional to temperature (Figure 2a), which is consistent with the behavior observed by Moore and Lockner (2013) for antigorite-quartz gouges. The antigorite-quartz gouges also show time-dependent weakening, which is more pronounced at higher temperatures, consistent with a delayed weakening related to temperature-dependent reaction kinetics. Moore and Lockner (2013) attribute this behavior to an increase in the effectiveness of solution-transfer processes at increased temperature. Mg-silicates (including serpentine) are more soluble in acidic fluids (Luce et al., 1972), and dissolution of quartz in a hydrous fluid consumes OH^- that is released during serpentine dissolution, resulting in a more acidic fluid (Moore & Lockner, 2013):

$$SiO_2 + H_2O + (OH)^- = (H_3SiO_4)^- \quad (1)$$

Therefore, the kinetics of solution-transfer processes involving antigorite should be faster in the presence of dissolving quartz (Moore & Lockner, 2013). The reaction of quartz and serpentine (a solution-transfer process) is known to form talc (Koons, 1981; Mori et al., 2007). Because of the frictional weakness of talc (Moore & Lockner, 2008), the rheology of serpentine-quartz faults has been suggested to be controlled by the growth of talc (Hirauchi et al., 2013).

Figure 5. Backscattered electron images and element maps of antigorite and antigorite-10% quartz samples. (a) Backscattered electron image of antigorite-only sample deformed at 500°C. Large, elongate antigorite clasts (marked A) are surrounded by a finer grained antigorite matrix with a kinked and folded foliation (dashed yellow lines). (b) and (c) Element maps of Mg and Si content of the same area as in panel (a). (d) Backscattered electron image of antigorite-10% quartz mixture, also deformed at 500°C. Antigorite foliation (dashed yellow lines) locally wraps around antigorite clasts (labeled A and, where lacking foliation, outlined in dashed white lines). Examples of minor quartz are labeled Q. (e) and (f) Element maps of relative variation in Mg and Si concentration in the same area as (d), small quartz grains (same examples as in panel (d)) are labeled Q and some antigorite examples are labeled A. (g) Backscattered electron image of antigorite +10% quartz deformed at room temperature. (h) Close-up of antigorite +10% quartz deformed at 500°C highlighting a rounded, asymmetric quartz grain (Q) with small pit (white arrow), antigorite clasts (A), and foliation along inferred dissolved antigorite grain boundaries (yellow arrows).

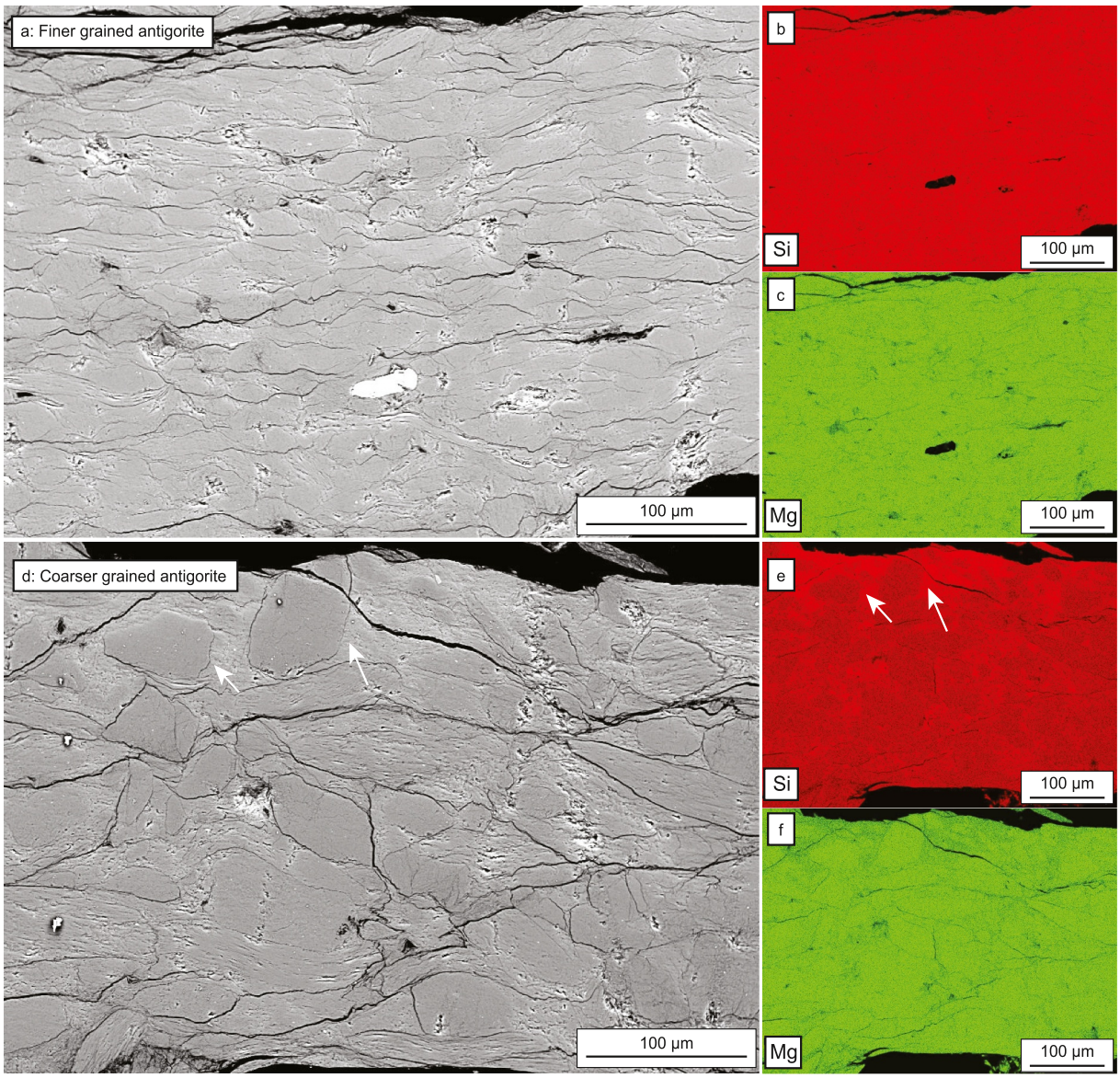

Figure 6. Microstructures of antigorite +5% quartz samples deformed at 500°C followed by room temperature deformation (experiment set b). (a) Backscattered electron image of a sample with initial antigorite grain size 25–45 μm (u870), where a scaly fabric developed. (b) and (c) Element maps showing relative concentrations of Si and Mg, with neither indicating any distinct remnant quartz. (d) Backscattered electron image of a sample with initial antigorite grain size 45–106 μm (u885), where some large, massive antigorite clasts are set in a foliated antigorite matrix. (e) and (f) Element maps showing relative concentrations of Si and Mg, indicating some elevated silica concentration along the top of the sample, particularly in stress shadows of large antigorite clasts (white arrows on (d) and (e)).

Although the presence of talc is implied by FTIR spectra of deformed samples (Figure 8), the microstructural context of this talc is unclear. Because talc has ∼20% more Si than serpentine per formula unit, higher Si concentrations detected adjacent to antigorite clasts in the STEM (Figures 7c and 7d) may reflect talc precipitated in stress shadows, where it may be localized and insufficiently interconnected to affect the bulk strength of the sample. There may also be some talc mixed with foliated antigorite and quartz matrix, but with grain size <1 μm as it is not resolved in the Bright field scanning transmitted electron microscopy imagery (Figures 5d–5f, 7a, and 7b). It may also be that some of the scattered Si indicates amorphous talc.

For mixtures with 5% quartz, fine-grained samples showed substantially lower strengths than coarser-grained samples at 500°C (Figure 2b), implying a grain-size sensitive deformation mechanism. For samples with 10% quartz deformed at 500°C, the grain size effect is smaller, but still detectable. When temperature was reduced from 500°C to room temperature; however, strength increased markedly in all samples (Figure 2b), implying that

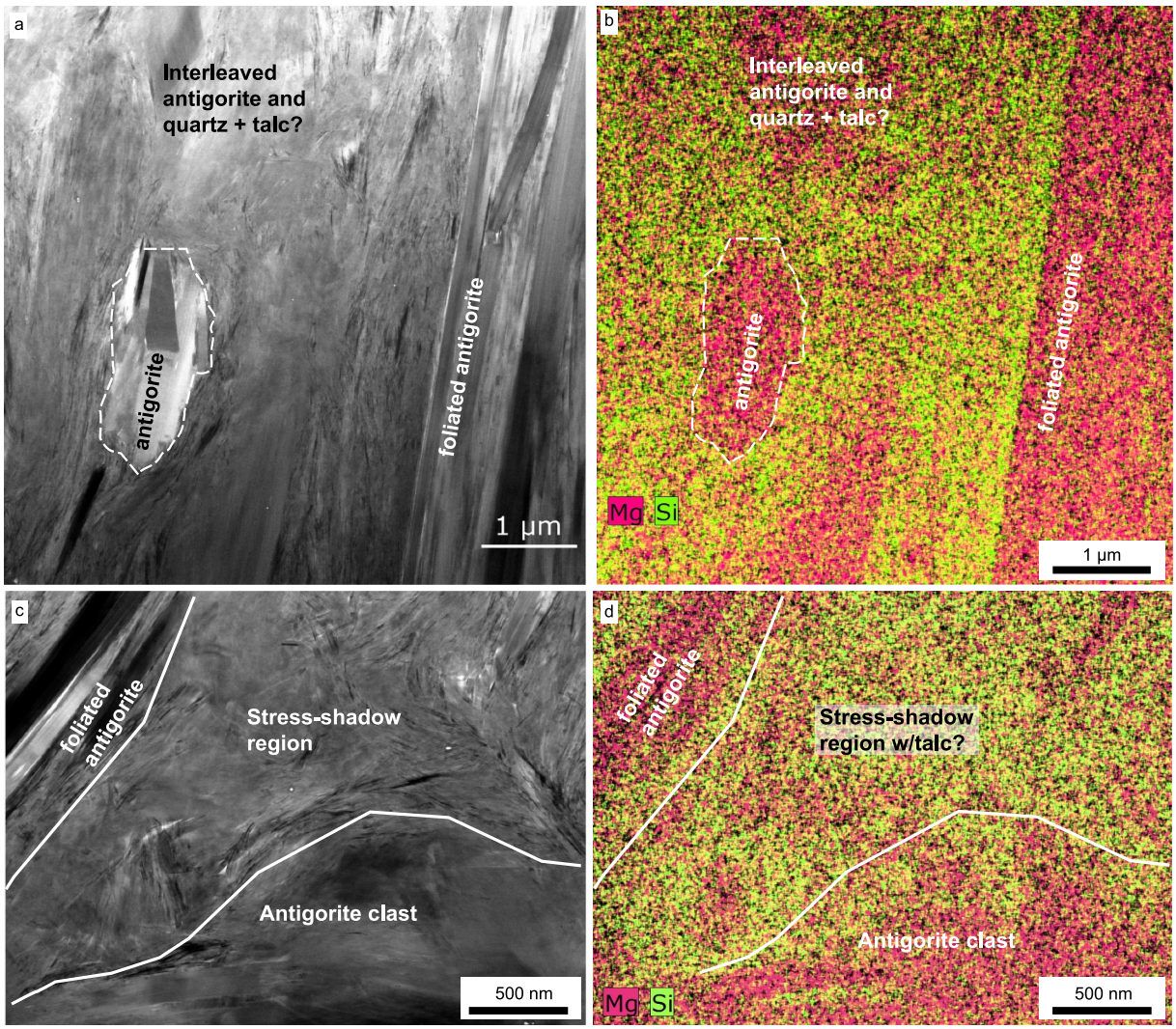

Figure 7. Bright field scanning transmitted electron microscopy (BF-STEM) images of sample u865, antigorite +10% quartz deformed at 500°C. (a) and (b) Area with a small antigorite clast surrounded by foliated, but locally folded and intercalated elongate mineral grains, neighboring a foliated zone at the righthand edge of the image. (b) Element map of the same area as (a). (c) BF-STEM image of a stress-shadow adjacent to an antigorite clast - characterized by fine grain size and variable mineral grain long axis orientations. (d) Element map of the same area as (c).

the rheology is temperature-dependent. Any talc formed at 500°C would still be present at room temperature, and we therefore infer that insufficient interconnected talc has formed to substantially weaken the cooled sample. Because talc has a low friction ($\leq$0.2) also at room temperature (Moore & Lockner, 2008), and our measured μ at room temperature is >0.3 for all experiments, we interpret that the rheology of antigorite-quartz mixtures at hydrothermal conditions is predominantly controlled by dissolution-precipitation creep of antigorite, rather than production of talc. Given this conclusion it is surprising that the grain-size dependence of antigorite with 10% quartz deformed at 500°C is very minor. However, it is important to realize that the measured shear stress combines contributions from dissolution-precipitation creep and frictional sliding over the foliation. Therefore, if dissolution-precipitation creep is easy and fast (relative to the strain rate), it will not contribute substantially to the overall shear stress and acceleration of the process due to a smaller grain size will not change the total shear stress much. Furthermore, we note that we only measured the initial grain size, and it is possible that grain size reduction during deformation reduced the difference in grain size between the samples.

At room temperature, the microstructure is cataclastic, and the friction coefficient is ~0.5. In these samples, shear is associated with fracture of clasts to create sliding surfaces and a fine grained matrix. In higher temperature experiments we infer that, as also concluded for natural examples deformed at T > 300°C (Liu et al., 2020; Tulley

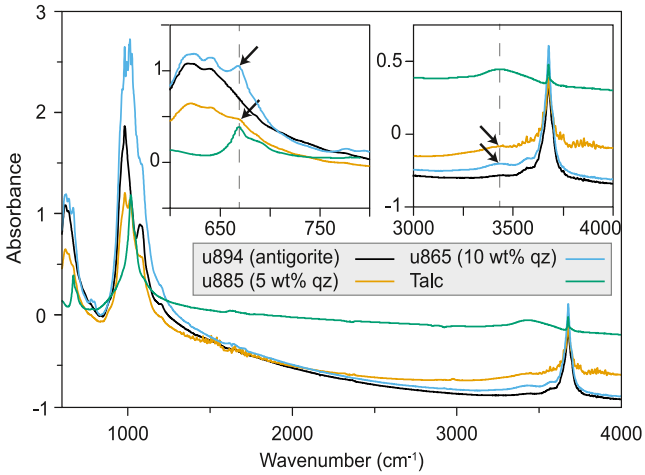

Figure 8. Fourier transform infrared spectra of deformed antigorite and antigorite-quartz mixtures, and a reference talc sample.

et al., 2022; Wassmann et al., 2011), shear is accommodated by sliding along antigorite (±talc) foliae, and shear surfaces are maintained by dissolution-precipitation creep removing any kinks or bends in the antigorite crystals. Shear therefore requires grain boundary (i.e., facet-on-facet) sliding also with a dissolution-precipitation mechanism (Gratier et al., 2023). This is reflected by a shear stress dependence on normal stress, seen in a normal stress stepping experiment performed at 500°C (Figure 3). We therefore interpret the deformation of antigorite-quartz at hydrothermal conditions as frictional-viscous creep (cf. Bos & Spiers, 2002). A frictional-viscous rheology for antigorite where dissolution-precipitation and facet-on-facet sliding operate in series has previously been proposed by Tulley et al. (2022) based on natural samples. We next explore this mechanism further with the experimental data.

4.2. Frictional-Viscous Flow

For quartz-antigorite experiments with 10% quartz, the same starting grain size range (45–106 μm) and conducted at equal sliding velocity (0.01 μm/s) and effective normal stress (150 MPa), we fitted the mechanical data to a creep equation for dissolution-precipitation creep. We neglect potential grain size reduction that occurred during shearing, which may lead us to overestimate strength. We assume that deformation occurred by frictional-viscous flow where total stress τ_{total} results from resistance to grain boundary sliding, τ_{gb}, and stress driving dissolution-precipitation creep τ_{dpc}.

$$\tau_{total} = \tau_{gb} + \tau_{dpc} \tag{2}$$

assuming these deformation processes are independent of each other. We assume τ_{gb} results from friction along aligned grain boundaries, so that

$$\tau_{gb} = \sigma_n' \mu_{gb} \tag{3}$$

where σ_n' is effective normal stress and μ_{gb} is the grain boundary friction coefficient. The shear strain rate accommodated by pressure solution can be expressed as (Rutter, 1976; Spiers et al., 1990):

$$\dot{\gamma}_{dpc} = \frac{AV_m}{RT}\frac{\tau_{dpc}}{d^p} \tag{4}$$

where A includes a dimensionless factor that depends on interface geometry as well as properties of the solvent and the dissolved solid, such as diffusivity, solubility, precipitation rate, and fluid film thickness, dependent on the rate-limiting step in the dissolution-precipitation process (e.g., Ashby & Verrall, 1973; Raj, 1982; Rutter, 1976; Shimizu, 1995). Because solubility and diffusivity are temperature-dependent, A will also depend on T. V_m is the molar volume of the solid (2.23×10^{-4} $m^3 mol^{-1}$ for antigorite), R is the universal gas constant, d is grain size (representing diffusive distance), and p is the grain size exponent, which also depends on the rate-limiting process. Diffusivity and solubility both have an Arrhenius dependence on temperature, so following Spiers et al. (1990) we can rewrite Equation 4 as

$$\dot{\gamma}_{dpc} = \frac{A_0 V_m}{RT}\exp\left(\frac{-\Delta H}{RT}\right)\frac{\tau_{dpc}}{d^p} \tag{5}$$

where ΔH is the activation energy. This formulation takes the temperature dependence out of A, and A_0 may therefore be constant among our group (a) experiments, where T is the only explicit variable and both normal stress and starting grain size range are kept constant. We assume the rate-limiting mechanism (among dissolution, precipitation, and diffusion), and therefore p, stays constant.

We obtain activation energy for shearing by dissolution-precipitation creep from Equation 5, by taking the negative slope of a best-fit line for $\ln T\dot{\gamma}/\tau_{dpc}$ plotted versus 1/RT (Figure 9a). This assumes that A_0, V_m, and d^p are

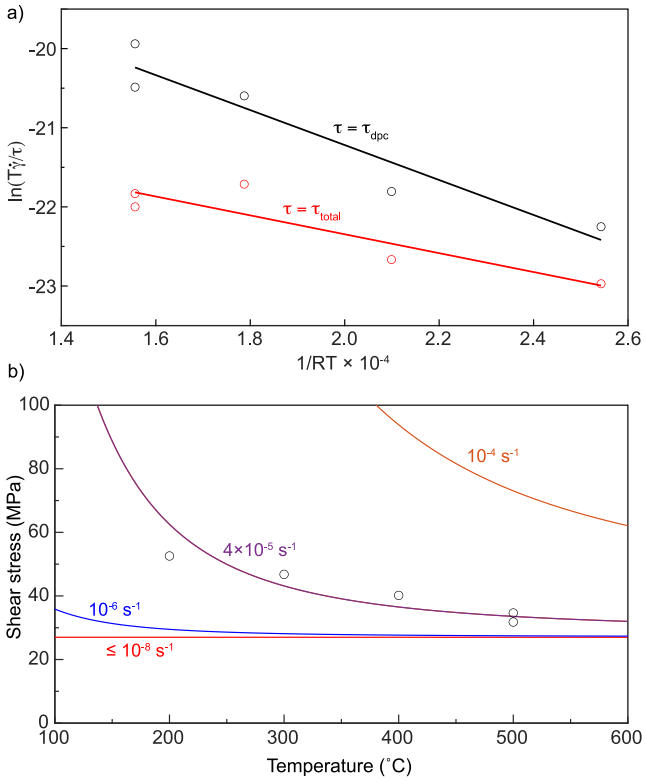

Figure 9. Plots fitting experimental data to constitutive relations. (a) Calculation of the activation energy for antigorite-quartz mixtures based on Equation 5. Red circles show the measured shear stress (τ_{total}). Black circles represent shear stress for dissolution-precipitation creep, defined as $\tau_{dpc} = \tau_{total} - \tau_{gb}$, where τ_{gb} is grain boundary friction assumed to be 0.18 for phyllosilicate facet-on-facet sliding. The activation energy when accounting for the effect of grain-boundary sliding ($\tau = \tau_{dpc}$) is 22 kJ mol^{-1}, with an R^2 value of 0.91, vs. $R^2 = 0.82$ for $\tau = \tau_{total}$. (b) Calculation of shear stress for frictional-viscous flow of antigorite with diffusion-limited dissolution-precipitation creep in the presence of quartz (Equation 2 with τ_{gb} from Equation 3 and τ_{dpc} from Equation 7). The relatively slight temperature dependence reflects a low activation energy of 22 kJ/mol. For strain rates $\leq 10^{-8}$ s^{-1} the shear stress for dissolution-precipitation creep becomes negligible and strength is essentially controlled by an assumed facet-on-facet frictional coefficient for antigorite and talc foliae of 0.18. All calculations assume the experimental effective normal stress of 150 MPa. The open circles are laboratory measurements. 4×10^{-5} s^{-1} is the average experimental strain rate assuming a deforming thickness of 800 μm and the imposed slip rate of 0.01 μm/s.

all constant. We measured deformed sample thickness as the difference between the piston length at the end of the experiment and the length of the empty piston set. We then obtained $\dot{\gamma}_{dpc}$ as the experimental slip rate of 0.01 μm/s divided by this sample thickness. This may be an underestimate if less than the full sample thickness participated in deformation; however, there is little evidence for shear localization in the microstructures. We also require an estimate of the frictional resistance to sliding along grain boundaries. We assume a μ_{gb} of 0.18, which is consistent with measurements of talc friction (Moore & Lockner, 2008) and could account for talc-lined grain boundaries assuming the talc-forming reaction is sufficiently effective. This is also comparable to the μ_{gb} of 0.16 we estimate from normal stress stepping at 500°C (Figure 3), and consistent with sliding along (001) facets in other phyllosilicate minerals at room temperature, such as muscovite (Kawai et al., 2015). However, significantly lower values have been obtained for (001) facet sliding in chlorite at 300°C (0.008; Okamoto et al., 2019), and muscovite at 600°C (0.08; Niemeijer, 2018), such that our calculated activation energy for dissolution-precipitation creep may be an overestimate.

From the calculation above, we obtain an activation energy of 22.1 kJ/mol for the antigorite-quartz mixtures (10% quartz) if $\tau = \tau_{dpc}$ (Figure 9a). The linear regression has an R^2 value of 0.91. In comparison, if we do not subtract the grain boundary friction from the measured stress (i.e., $\tau = \tau_{total}$), we obtain a lower activation energy of 11.9 kJ/mol and a poorer linear regression fit with $R^2 = 0.82$.

An activation energy of 22 kJ/mol for a dissolution-precipitation creep component of frictional-viscous flow is low relative to values of 49–77 kJ/mol for silica-water reactions, which are limited by breaking of strong Si-O bonds (Rimstidt & Barnes, 1980). It is also lower than values of 34–83 kJ/mol obtained for pure antigorite undergoing semibrittle deformation in deformation experiments at pressures exceeding 1 GPa (Shao et al., 2021). The activation energy calculated from our antigorite-quartz experiments is, however, comparable to a value of 15 kJ/mol determined by Nakashima (1995) for the activation energy of ion diffusion in an aqueous grain boundary film. An apparent activation energy of 18 kJ/mol has also been estimated for subduction-related, diffusion-limited pressure solution in shales in the Shimanto Complex of Japan, based on microstructure of naturally deformed rock (Kawabata et al., 2007). Thus, this activation energy is similar to estimates for diffusion-limited dissolution-precipitation creep, but lower than that for precipitation/dissolution of silica phases and higher-pressure semibrittle flow of antigorite.

4.3. Implications for Natural Shear Zones

We conclude that our results provide experimental evidence that dissolution-precipitation creep can operate in antigorite serpentine. This mechanism, interpreted to operate in series with facet-on-facet sliding, results in an overall frictional-viscous rheology. The low activation energy of 22 kJ/mol calculated above leads us to infer that dissolution-precipitation creep is diffusion-limited in these experiments. Since we conducted the majority of our experiments with the same grain size, we are unable to accurately constrain the grain-size exponent, to test whether $p = 3$ as predicted for diffusion along grain boundaries (e.g., Karato, 2008, Chapter 8). Assuming diffusion-limited pressure solution, we can elaborate on Equation 4 so that (Rutter, 1976; Spiers et al., 1990):

$$\dot{\gamma}_{dpc} = \frac{BV_m}{RT} DCS \frac{\tau_{dpc}}{d^3} \quad (6)$$

where B is a non-dimensional geometric factor for shear deformation (typical value of 100; Ashby & Verrall, 1973; Rutter, 1976), and DCS is a product of diffusivity, solubility, and thickness of the grain boundary fluid film, respectively. D and C have an Arrhenius dependence on temperature, so following Spiers et al. (1990) we can rewrite the equation as

$$\dot{\gamma}_{dpc} = \frac{BV_m}{RT} Z_0 \exp\left(\frac{-\Delta H}{RT}\right) \frac{\tau_{dpc}}{d^3} \tag{7}$$

where $Z_0 = D_0 C_0 S$ is the product DCS at the limit where $1/T \rightarrow 0$. We derive a value of $Z_0 = (8 \pm 2) \times 10^{-18}$ m^3/s by applying Equation 7 to each experiment at 150 MPa normal stress and grain size range 45–106 μm, using a mid-range grain size of 75 μm, $\dot{\gamma}$ as per measured sample thickness, and $\Delta H = 22$ kJ/mol. We are not aware of any antigorite diffusion data we can compare this result to, but note it is three orders of magnitude lower than Z_0 derived for flow of rocksalt by diffusion-limited pressure solution (Spiers et al., 1990).

We use Equation 2 with τ_{gb} from Equation 3 and τ_{dpc} from Equation 7 to calculate the relationship between temperature and total shear stress for a range of strain rates (Figure 9b). We make these calculations for an effective normal stress of 150 MPa, as in the experiments, and a grain size of 75 μm which is the mid-value of the initial experimental grain size range. This is likely an overestimate given probable grain size reduction during shear. Extrapolating to natural strain rates, we find that the low activation energy and calculated Z_0 give negligible resistance to flow by dissolution-precipitation creep at strain rates of 10^{-8} s^{-1} or slower. At natural strain rates, the strength of antigorite in the presence of quartz undergoing dissolution is therefore expected to be very low, and controlled by the grain boundary friction in foliated shear zones. This is not surprising given the laboratory results, which indicate that as temperature increases, most of the strength is supported by the requisite accommodation mechanism for dissolution-precipitation creep, which is interpreted to be facet-on-facet sliding. At lower natural strain rates, grain boundary diffusion is faster relative to the deformation rate.

While Equation 7 fits the experiments at $T \geq 200$°C well (Figure 9b), it is uncertain how confidently the experimentally determined parameters can be extrapolated. We have assumed no effects of porosity or strain, and both Z_0 and ΔH may have a normal stress dependence that we have not explored. Given that the experiment at room temperature is stronger than we have assumed for facet-on-facet sliding, but weaker than expected from extrapolating a diffusion-limited pressure solution flow law to room temperature, another process is controlling strength in this sample. Given the cataclastic microstructure, this is probably fracture and sliding on new surfaces that are not parallel to foliation - a process that is known to give approximately Byerlee friction for antigorite (e.g., Tesei et al., 2018). This, however, implies there is a minimum temperature below which diffusion is no longer efficient.

The stresses required for dissolution-precipitation creep of antigorite (without quartz), particularly at natural strain rates, remain uncertain. However, considering that the principal effect of quartz is to increase antigorite solubility and rate of dissolution (Moore & Lockner, 2013), and solubility is contained within the constant Z_0, decreasing solubility by an order of magnitude should result in an order of magnitude increase in driving stress. As the calculated driving stresses for dissolution-precipitation of antigorite-quartz mixtures are quite low, a decrease in solubility by several orders of magnitude may, however, be sustainable before driving stresses are large enough to cause a transition to cataclasis, particularly in nature. In the lab, however, one or two order of magnitude increase in shear stress would potentially make dissolution-precipitation creep unachievable (Figure 9b), and cataclasis or dislocation creep be recorded instead, as is commonly the case.

Although dissolution-precipitation creep makes a negligible contribution to bulk strength at natural strain rates, it allows geometrical asperities to be removed, allowing for continuous facet-on-facet sliding (as illustrated in Figure 5 of Tulley et al., 2022). Without dissolution-precipitation creep, continual sliding of a well-aligned aggregate will lead to the development of micro-scale folds, presenting geometrical asperities. Such geometrical asperities, which develop with progressive strain in phyllosilicate-rich gouges, cause driving stresses to increase (Niemeijer, 2018; Okamoto et al., 2019). This situation is analogous to cases where driving stresses are increased externally, for example, by increasing strain rate.

In general, when the ability of dissolution-precipitation creep to resolve geometrical asperities decreases, cataclasis becomes a more important deformation mechanism (Bos & Spiers, 2002). We interpret this to be the reason

for stick-slip in experiments with pure antigorite at 500°C. In nature, blocks of serpentinite with interlocking crystals, which generally have a coarser grain size and are likely relatively impermeable, commonly have a greater intensity of fracturing compared to enveloping foliated serpentine that may have elevated, foliation-parallel, permeability and generally finer grain size (e.g., Cox et al., 2021; Tarling et al., 2019; Tulley et al., 2022). Note that an order of magnitude increase in grain size would lead to three orders of magnitude increase in stress (Equation 7). Stick-slip in nature, at ambient plate boundary strain rates, may therefore be limited to dry, impermeable, coarser-grained serpentinite with limited length scale, whereas dissolution-precipitation creep is predicted to dominate where fluid infiltration (assuming favorable pH) allows diffusion-controlled dissolution-precipitation creep and frictional-viscous flow.

On geological timescales, chemical reaction might lead to an interconnected talc layer forming between serpentine and quartz-rich lithologies. However, at plate boundary strain rates, the strength required to deform antigorite by dissolution-precipitation creep coupled to facet-on-facet sliding may be comparable or less than that required for frictional slip within a talc layer. Overall, our results give strong support to a frictional-viscous rheology for antigorite at hydrothermal conditions and natural, steady tectonic strain rates. However, note that this rheology, as well as a potential transition to a talc-dominated rheology, requires a fluid to be available. Such a mechanism of fluid-dependent weakening and frictional stability has been proposed for serpentine by previous field studies on antigorite (Tulley et al., 2022; Wassmann et al., 2011) as well as lizardite-chrysotile serpentine (Andréani et al., 2005; Cox et al., 2021; Tarling et al., 2019), and might therefore be widespread in nature.

5. Conclusion

Hydrothermal ring-shear experiments deforming antigorite and antigorite-quartz mixtures show that presence of quartz has a significant weakening effect on antigorite rheology. Experiments without quartz produced friction coefficients similar to most crustal rocks, led to stick-slip behavior at high temperature, and generated cataclastic microstructures indicative of frictional behavior. In contrast, antigorite-quartz gouges showed stable sliding and substantially lower strengths that are inversely proportional to temperature and both normal stress and grain size-dependent, consistent with a solution-transfer process controlling strength in tandem with grain boundary (i.e., facet-on-facet) sliding. We suggest that the presence of quartz in antigorite gouge under hydrothermal conditions enhances the chemical kinetics of dissolution-precipitation creep, allowing this mechanism to operate at laboratory strain rates. As suggested by Moore and Lockner (2013), this is likely an effect of enhanced solubility of antigorite in a pore fluid buffered by dissolution of quartz. Minor talc also formed in the experiment, but is not observed to have developed through-going connectivity, nor does it appear to markedly affect bulk strength, which remains high when samples are returned to room temperature.

We calculate an activation energy of 22 kJ/mol for dissolution-precipitation creep in the experimental samples, which we infer is the activation energy for grain boundary diffusion in antigorite, at conditions where dissolution is fast and not rate-limiting. This result suggests that frictional-viscous flow involving dissolution-precipitation creep can be a significant deformation mechanism in natural antigorite shear zones under conditions where fluid is available and solubility is sufficiently high. Natural, sufficiently permeable, antigorite shear zones may therefore be significantly weaker in the presence of quartz, or at slow strain rates where dissolution and diffusion are sufficiently fast relative to deformation rates, such that frictional-viscous flow is able to occur.

Acknowledgments
We appreciate constructive comments from Haemyeong Jung and an anonymous reviewer. The work was supported by the European Union's Horizon 2020 research and innovation program (Starting Grant 715836 "MICA" to ÅF). Thony van de Gon-Netscher of Utrecht University is thanked for technical support with the ring-shear apparatus, Leonard Bik is thanked for thin section preparation. ÅF also acknowledges support from the project FricFrac funded by the Center for Advanced Study at the Norwegian Academy of Science and Letters during academic year 2023–2024.

Data Availability Statement

The experimental results the paper is based on are available from Niemeijer (2024).

References

Andréani, M., Boullier, A.-M., & Gratier, J.-P. (2005). Development of schistosity by dissolution–crystallization in a Californian serpentinite gouge. *Journal of Structural Geology*, *27*(12), 2256–2267. https://doi.org/10.1016/j.jsg.2005.08.004

Ashby, M. F., & Verrall, R. A. (1973). Diffusion accommodated flow and superplasticity. *Acta Metallurgica*, *21*(2), 149–163. https://doi.org/10.1016/0001-6160(73)90057-6

Balan, E., Fritsch, E., Radtke, G., Paulatto, L., Juillot, F., & Petit, S. (2021). First-principles modeling of the infrared spectrum of antigorite. *European Journal of Mineralogy*, *33*(4), 389–400. https://doi.org/10.5194/ejm-33-389-2021

Blenkinsop, T. G. (2007). *Deformation microstructures and mechanisms in minerals and rocks*. Springer Science & Business Media.

Bos, B., & Spiers, C. J. (2002). Frictional-viscous flow of phyllosilicate-bearing fault rock: Microphysical model and implications for crustal strength profiles. *Journal of Geophysical Research*, *107*(B2), ECV–1. https://doi.org/10.1029/2001jb000301

Burdette, E., & Hirth, G. (2022). Creep rheology of antigorite: Experiments at subduction zone conditions. *Journal of Geophysical Research: Solid Earth*, *127*(7), e2022JB024260. https://doi.org/10.1029/2022jb024260

Byerlee, J. (1978). Friction of rocks. In *Rock friction and earthquake prediction* (pp. 615–626). Springer.

Chernak, L. J., & Hirth, G. (2010). Deformation of antigorite serpentinite at high temperature and pressure. *Earth and Planetary Science Letters*, *296*(1–2), 23–33. https://doi.org/10.1016/j.epsl.2010.04.035

Cox, S., Fagereng, Å., & MacLeod, C. J. (2021). Shear zone development in serpentinized mantle: Implications for the strength of oceanic transform faults. *Journal of Geophysical Research: Solid Earth*, *126*(5), e2020JB020763. https://doi.org/10.1029/2020jb020763

Fagereng, Å., & Biggs, J. (2019). New perspectives on 'geological strain rates' calculated from both naturally deformed and actively deforming rocks. *Journal of Structural Geology*, *125*, 100–110. https://doi.org/10.1016/j.jsg.2018.10.004

French, M. E., Hirth, G., & Okazaki, K. (2019). Fracture-induced pore fluid pressure weakening and dehydration of serpentinite. *Tectonophysics*, *767*, 228168. https://doi.org/10.1016/j.tecto.2019.228168

Goswami, A., & Barbot, S. (2018). Slow-slip events in semi-brittle serpentinite fault zones. *Scientific Reports*, *8*(1), 6181. https://doi.org/10.1038/s41598-018-24637-z

Gratier, J.-P., Menegon, L., & Renard, F. (2023). Pressure solution grain boundary sliding as a large strain mechanism of superplastic flow in the upper crust. *Journal of Geophysical Research: Solid Earth*, *128*(4), e2022JB026019. https://doi.org/10.1029/2022JB026019

Hansen, L. N., David, E. C., Brantut, N., & Wallis, D. (2020). Insight into the microphysics of antigorite deformation from spherical nano-indentation. *Philosophical Transactions of the Royal Society A*, *378*(2165), 20190197. https://doi.org/10.1098/rsta.2019.0197

Hilairet, N., Reynard, B., Wang, Y., Daniel, I., Merkel, S., Nishiyama, N., & Petitgirard, S. (2007). High-pressure creep of serpentine, interseismic deformation, and initiation of subduction. *Science*, *318*(5858), 1910–1913. https://doi.org/10.1126/science.1148494

Hirauchi, K., den Hartog, S. A. M., & Spiers, C. J. (2013). Weakening of the slab–mantle wedge interface induced by metasomatic growth of talc. *Geology*, *41*(1), 75–78. https://doi.org/10.1130/g33552.1

Hirauchi, K., Katayama, I., & Kouketso, Y. (2020). Semi-brittle deformation of antigorite serpentinite under forearc mantle wedge conditions. *Journal of Structural Geology*, *140*, 104151. https://doi.org/10.1016/j.jsg.2020.104151

Hirauchi, K., Nagata, Y., Kataoka, K., Oyanagi, R., Okamoto, A., & Michibayashi, K. (2021). Cataclastic and crystal-plastic deformation in shallow mantle-wedge serpentinite controlled by cyclic changes in pore fluid pressures. *Earth and Planetary Science Letters*, *576*, 117232. https://doi.org/10.1016/j.epsl.2021.117232

Karato, S.-i. (2008). Deformation of earth materials. *An introduction to the rheology of Solid Earth*, *463*.

Kawabata, K., Tanaka, H., & Kimura, G. (2007). Mass transfer and pressure solution in deformed shale of accretionary complex: Examples from the Shimanto Belt, southwest Japan. *Journal of Structural Geology*, *29*(4), 697–711. https://doi.org/10.1016/j.jsg.2006.11.009

Kawai, K., Sakuma, H., Katayama, I., & Tamura, K. (2015). Frictional characteristics of single and polycrystalline muscovite and influence of fluid chemistry. *Journal of Geophysical Research: Solid Earth*, *120*(9), 6209–6218. https://doi.org/10.1002/2015jb012286

Koons, P. O. (1981). A study of natural and experimental metasomatic assemblages in an ultramafic-quartzofeldspathic metasomatic system from the Haast Schist, South Island, New Zealand. *Contributions to Mineralogy and Petrology*, *78*(2), 189–195. https://doi.org/10.1007/bf00373780

Liu, W., Zhang, J., Cao, Y., & Jin, Z. (2020). Geneses of two contrasting antigorite crystal preferred orientations and their implications for seismic anisotropy in the forearc mantle. *Journal of Geophysical Research: Solid Earth*, *125*(9), e2020JB019354. https://doi.org/10.1029/2020jb019354

Luce, R. W., Bartlett, R. W., & Parks, G. A. (1972). Dissolution kinetics of magnesium silicates. *Geochimica et Cosmochimica Acta*, *36*(1), 35–50. https://doi.org/10.1016/0016-7037(72)90119-6

Moore, D. E., & Lockner, D. A. (2008). Talc friction in the temperature range 25°–400°C: Relevance for fault-zone weakening. *Tectonophysics*, *449*(1–4), 120–132. https://doi.org/10.1016/j.tecto.2007.11.039

Moore, D. E., & Lockner, D. A. (2013). Chemical controls on fault behavior: Weakening of serpentinite sheared against quartz-bearing rocks and its significance for fault creep in the San Andreas system. *Journal of Geophysical Research: Solid Earth*, *118*(5), 2558–2570. https://doi.org/10.1002/jgrb.50140

Mori, Y., Nishiyama, T., & Yanagi, T. (2007). Chemical mass balance in a reaction zone between serpentinite and metapelites in the Nishisonogi metamorphic rocks, Kyushu, Japan: Implications for devolatilization. *Island Arc*, *16*(1), 28–39. https://doi.org/10.1111/j.1440-1738.2007.00556.x

Nakashima, S. (1995). Diffusivity of ions in pore-water as a quantitative basis for rock deformation rate estimates. *Tectonophysics*, *245*(3–4), 185–203. https://doi.org/10.1016/0040-1951(94)00234-z

Niemeijer, A. R. (2018). Velocity-dependent slip weakening by the combined operation of pressure solution and foliation development. *Scientific Reports*, *8*(1), 1–10. https://doi.org/10.1038/s41598-018-22889-3

Niemeijer, A. R. (2024). *Dataset for: Activation of dissolution-precipitation creep causes weakening and viscous behaviour in experimentally-deformed antigorite* (Tech. Rep.). Utrecht University. https://doi.org/10.24416/UU01-94P4HL

Niemeijer, A. R., Spiers, C. J., & Peach, C. J. (2008). Frictional behaviour of simulated quartz fault gouges under hydrothermal conditions: Results from ultra-high strain rotary shear experiments. *Tectonophysics*, *460*(1–4), 288–303. https://doi.org/10.1016/j.tecto.2008.09.003

Okamoto, A. S., Verberne, B. A., Niemeijer, A. R., Takahashi, M., Shimizu, I., Ueda, T., & Spiers, C. J. (2019). Frictional properties of simulated chlorite gouge at hydrothermal conditions: Implications for subduction megathrusts. *Journal of Geophysical Research: Solid Earth*, *124*(5), 4545–4565. https://doi.org/10.1029/2018jb017205

Okazaki, K., & Katayama, I. (2015). Slow stick slip of antigorite serpentinite under hydrothermal conditions as a possible mechanism for slow earthquakes. *Geophysical Research Letters*, *42*(4), 1099–1104. https://doi.org/10.1002/2014GL062735

Padrón-Navarta, J. A., Tommasi, A., Garrido, C. J., & Sánchez-Vizcaíno, V. L. (2012). Plastic deformation and development of antigorite crystal preferred orientation in high-pressure serpentinites. *Earth and Planetary Science Letters*, *349*, 75–86. https://doi.org/10.1016/j.epsl.2012.06.049

Parry, S. A., Pawley, A. R., Jones, R. L., & Clark, S. M. (2007). An infrared spectroscopic study of the OH stretching frequencies of talc and 10-Å phase to 10 GPa. *American Mineralogist*, *92*(4), 525–531. https://doi.org/10.2138/am.2007.2211

Peacock, S. M., & Hyndman, R. D. (1999). Hydrous minerals in the mantle wedge and the maximum depth of subduction thrust earthquakes. *Geophysical Research Letters*, *26*(16), 2517–2520. https://doi.org/10.1029/1999gl900558

Proctor, B., & Hirth, G. (2016). "Ductile to brittle" transition in thermally stable antigorite gouge at mantle pressures. *Journal of Geophysical Research: Solid Earth*, *121*(3), 1652–1663. https://doi.org/10.1002/2015jb012710

Raj, R. (1982). Creep in polycrystalline aggregates by matter transport through a liquid phase. *Journal of Geophysical Research*, *87*(B6), 4731–4739. https://doi.org/10.1029/jb087ib06p04731

Reinen, L. A., Weeks, J. D., & Tullis, T. E. (1994). The frictional behavior of lizardite and antigorite serpentinites: Experiments, constitutive models, and implications for natural faults. *Pure and Applied Geophysics*, *143*(1), 317–358. https://doi.org/10.1007/bf00874334

Rimstidt, J. D., & Barnes, H. L. (1980). The kinetics of silica-water reactions. *Geochimica et Cosmochimica Acta*, *44*(11), 1683–1699. https://doi.org/10.1016/0016-7037(80)90220-3

Rutter, E. H. (1976). The kinetics of rock deformation by pressure solution. *Philosophical Transactions of the Royal Society of London*, *283*, 203–219.

Shao, T., Zhou, Y., Song, M., Ma, X., Zhang, L., Yao, W., et al. (2021). Deformation of antigorite and its geological implications. *Journal of Geophysical Research: Solid Earth*, *126*(6), e2021JB021650. https://doi.org/10.1029/2021jb021650

Shimizu, I. (1995). Kinetics of pressure solution creep in quartz: Theoretical considerations. *Tectonophysics*, *245*(3–4), 121–134. https://doi.org/10.1016/0040-1951(94)00230-7

Spiers, C. J., Schutjens, P. M. T. M., Brzesowsky, R. H., Peach, C. J., Liezenberg, J. L., & Zwart, H. J. (1990). *Experimental determination of the constitutive parameters governing creep of rocksalt by pressure solution* (Vol. 54, pp. 215–227). Geological Society of London Special Publications.

Takahashi, M., Uehara, S.-I., Mizoguchi, K., Shimizu, I., Okazaki, K., & Masuda, K. (2011). On the transient response of serpentine (antigorite) gouge to stepwise changes in slip velocity under high-temperature conditions. *Journal of Geophysical Research*, *116*(B10), B10405. https://doi.org/10.1029/2010jb008062

Tarling, M. S., Smith, S. A. F., Scott, J. M., Rooney, J. S., Viti, C., & Gordon, K. C. (2019). The internal structure and composition of a plate-boundary-scale serpentinite shear zone: The Livingstone Fault, New Zealand. *Solid Earth*, *10*(4), 1025–1047. https://doi.org/10.5194/se-10-1025-2019

Tesei, T., Harbord, C. W. A., De Paola, N., Collettini, C., & Viti, C. (2018). Friction of mineralogically controlled serpentinites and implications for fault weakness. *Journal of Geophysical Research: Solid Earth*, *123*(8), 6976–6991. https://doi.org/10.1029/2018jb016058

Tulley, C. J., Fagereng, Å., Ujiie, K., Piazolo, S., Tarling, M. S., & Mori, Y. (2022). Rheology of naturally deformed antigorite serpentinite: Strain and strain-rate dependence at mantle-wedge conditions. *Geophysical Research Letters*, *49*(16), e2022GL098945. https://doi.org/10.1029/2022gl098945

Ulmer, P., & Trommsdorff, V. (1995). Serpentine stability to mantle depths and subduction-related magmatism. *Science*, *268*(5212), 858–861. https://doi.org/10.1126/science.268.5212.858

Wada, I., & Wang, K. (2009). Common depth of slab-mantle decoupling: Reconciling diversity and uniformity of subduction zones. *Geochemistry, Geophysics, Geosystems*, *10*(10). https://doi.org/10.1029/2009gc002570

Wang, K., Huang, T., Tilmann, F., Peacock, S. M., & Lange, D. (2020). Role of Serpentinized mantle wedge in affecting Megathrust Seismogenic behavior in the area of the 2010 M= 8.8 Maule earthquake. *Geophysical Research Letters*, *47*(22), e2020GL090482. https://doi.org/10.1029/2020gl090482

Warren, J. M., & Hirth, G. (2006). Grain size sensitive deformation mechanisms in naturally deformed peridotites. *Earth and Planetary Science Letters*, *248*(1–2), 438–450. https://doi.org/10.1016/j.epsl.2006.06.006

Wassmann, S., Stöckhert, B., & Trepmann, C. A. (2011). Dissolution precipitation creep versus crystalline plasticity in high-pressure metamorphic serpentinites. *Geological Society, London, Special Publications*, *360*(1), 129–149. https://doi.org/10.1144/sp360.8